Thermochimica Acta, 210 (1992) 103–121
Elsevier Science Publishers B.V., Amsterdam

Characterization of the thermal genesis course of manganese oxides from inorganic precursors

A.K.H. Nohman [a], M.I. Zaki [a], S.A.A. Mansour [a], R.B. Fahim [a] and C. Kappenstein [b]

[a] *Chemistry Department, Faculty of Science, Minia University, El-Minia 61519 (Egypt)*
[b] *Catalyse en Chimie Organique, Faculté des Sciences de Poitiers, 86022 Poitiers Cédex (France)*

(Received 3 March 1992)

Abstract

NH_4MnO_4, Mn_3O_4 and $Mn(NO_3)_2 \cdot 6H_2O$ were used as precursor compounds for the thermal genesis (at 150–600°C) of manganese oxides. Thermal events occurring during the genesis course were monitored by means of thermogravimetry and differential thermal analysis, in oxidizing and non-oxidizing atmospheres. Intermediate and final solid-phase products were characterized using X-ray diffractometry and infrared spectroscopy. Model manganese oxides were subjected to similar examinations for reference purposes. The results indicated that NH_4MnO_4 is almost completely decomposed near 120°C, giving rise to predominantly α-Mn_2O_3. The presence of K^+ contaminant supports an oxidative conversion of α-Mn_2O_3 into KMn_8O_{16} at $\geq$300°C. In contrast, the genesis of pure α-Mn_2O_3 from $Mn(NO_3)_2 \cdot 6H_2O$ is not achieved unless the calcination temperature exceeds 500°C; β-MnO_2 was the only detectable intermediate. Mn_3O_4, obtained at room temperature by the addition of aqueous Mn^{2+} to ammonia solution, was converted into α-Mn_2O_3 via the formation and subsequent decomposition of Mn_5O_8 at $\geq$300°C.

INTRODUCTION

Manganese oxides (MnO_x) are important catalytic [1–3] and electrochemical [4, 5] materials. In both applications, their performance is critically controlled by the chemical and phase compositions of the material [6, 7].

MnO_x usually occurs in one of the following stoichiometries: MnO, Mn_3O_4, Mn_2O_3 and MnO_2 [6, 8]. Thus, x has values from 1 to 2, and the Mn oxidation states range from 2+ to 4+. These oxides are variously structured [9]. Moreover, each of them may exist in different structural modifications, and have disparate degrees of non-stoichiometry [7, 9]. The ability of MnO_x to take up excess oxygen has long been investigated [10].

Correspondence to: C. Kappenstein, Catalyse en Chimie Organique, Faculté des Sciences de Poitiers, 86022 Poitiers Cédex, France.

It has been established [10, 11] that MnO can take in oxygen up to $MnO_{1.13}$, Mn_3O_4 up to $MnO_{1.42}$ and Mn_2O_3 up to $MnO_{1.58}$, without any apparent change in the lattice. In contrast, MnO_2 cannot lose any oxygen without the appearance of the Mn_2O_3 lattice. Thus, well-defined mixed-valency MnO_x oxides have been synthesized and characterized; e.g. Mn_5O_8 ($Mn_2^{2+}Mn_3^{4+}O_8$, manganoxide) [12].

It has also been established [8, 13], that the composition and structure of synthetic MnO_x are largely dependent of the preparation variables, namely, the method, precursor compound and thermal pre-treatment conditions. However, most of the studies performed in this field (refs. 8, 13, and references cited therein) have depended on examinations that have concentrated on the end products.

Therefore, the present study basically investigates the thermal genesis course of MnO_x from inorganic precursors, and correlates the physicochemical characteristics of the products with the thermal events encountered. To accomplish these objectives (i) $Mn(NO_3)_2 \cdot 6H_2O$, NH_4MnO_4 and $MnO_x(OH)_y$ were the precursor compounds used, the latter two somewhat unusually; (ii) the thermal events occurring during the precursor decomposition were monitored by means of thermogravimetry and differential thermal analysis; (iii) the decomposition products were characterized by means of X-ray diffractometry and infrared spectroscopy; and (iv) model MnO_x compounds were similarly characterized for reference purposes.

EXPERIMENTAL

Precursor compounds

Three precursor compounds were used: manganous nitrate, $Mn(NO_3)_2 \cdot 6H_2O$; manganic oxyhydroxide (or so believed to be), $MnO_x(OH)_y$; and ammonium permanganate, NH_4MnO_4. They are denoted respectively **MnII**, **MnIII** and **MnVII**. **MnII** was an AR grade Merck product, whereas **MnIII** and **MnVII** were synthesized. **MnIII** was obtained by a drop-wise addition of a 0.3 M aqueous solution of $Mn(NO_3)_2 \cdot 6H_2O$ to an aqueous ammonia solution (pH 9, about 6 M) at room temperature and in ambient atmosphere of air, with constant stirring. A light brown precipitate was formed, which was left overnight in contact with the mother liquor, filtered without washing, and dried at 25°C and 10^{-2} Torr. **MnVII** was synthesized via a metathetical reaction between $KMnO_4$ and NH_4Cl, according to Bircumshaw and Taylor [14].

Each of the precursors was calcined at 150, 300 and 600°C for 5 h; the calcination temperatures were chosen in view of the thermal analysis results (see below). In the case of **MnVII**, the starting material was not NH_4MnO_4 but its decomposition product obtained by heating slowly

(2°C min^{-1}) up to 120°C. This pre-treatment was carried out to avoid the explosive decomposition of NH_4MnO_4 when heated rapidly [15].

For convenience, the calcination products are indicated by a combination of the precursor designation and the calcination temperature in parentheses; thus, **MnII(300)** means the calcination product of $Mn(NO_3)_2 \cdot 6H_2O$ at 300°C for 5 h.

Model oxides

MnO, Mn_2O_3, Mn_3O_4 and MnO_2 were the model oxides employed, AR grade, Strem Chemicals Inc. (USA), and were used as purchased.

Thermogravimetry (TG) and differential thermal analysis (DTA)

TG and DTA curves were measured between room temperature and 700°C, at 10°C min^{-1} and in a dynamic atmosphere of air or N_2 (20 ml min^{-1}), using an automatically recording model 30H Shimadzu analyser (Japan). Small portions (10–15 mg) of the test samples were used for the TG, and α-Al_2O_3 was the reference material for the DTA.

X-ray diffractometry (XRD)

XRD powder diffractograms were recorded step-wise (0.02°, 1 s) at room temperature with a Siemens D500 diffractometer (Germany), equipped with a copper anode generating Cu Kα_{1+2} radiation (λ = 1.5418 Å; 40 kV, 30 mA; back monochromator), in the 2θ range between 5 and 80°, with a divergence slit of 1°. An on-line PC-AT microcomputer facilitated data acquisition and handling. For phase identification purposes, automatic JCPDS library search (standard SEARCH software, Sietronic/Australia) and match (standard EVA software, Socabim/France) were also used.

Infrared spectroscopy (IR)

IR absorption spectra were taken from KBr-supported test samples (<1 wt.%), over the frequency range 4000–200 cm^{-1} and at a resolution of 4 cm^{-1}, using a model 510 Nicolet Fourier-transform spectrophotometer (USA). A built-in data station facilitated spectra acquisition and handling.

RESULTS

Model oxides

The XRD and IR analyses results obtained for the model Mn oxides (MnO, Mn_3O_4, Mn_2O_3 and MnO_2) are summarized in Table 1. Table 2

TABLE 1

Characteristic XRD and IR results of model Mn oxides

Oxide	XRD			IR [a]	
	2θ (°)	d (Å)	I/I_0	ν (cm^{-1})	Description
MnO	40.712	2.2144	100	345	vs
	58.870	1.5674	58	462	vs, sh
	35.083	2.5558	53	560	m, sh
	70.320	1.3376	23		
Mn_3O_4	36.180	2.4808	100	320	m, sh
	32.359	2.7644	93	352	m, sp
	59.945	1.5419	46	419	s, sp
	28.929	3.0839	44	499	vs
				616	vs
				980	w, b
Mn_2O_3	32.993	2.7127	100	291	w, sp
	55.240	1.6615	22	397	m, sh
	23.160	3.8374	15	445	s, sh
	38.289	2.3488	13	501	vs, sh
				523	vs, sp
				574	vs, sp
				599	s, sh
				666	s
MnO_2	28.728	3.1050	100	343	m, sp
	59.480	1.5528	10	405	s, sp
	41.054	2.1968	9	545	vs
	56.780	1.6201	9	675	s
				710	m, sh

[a] Key: vs, very strong; s, strong; m, medium; w, weak; b, broad; sp, sharp; sh, shoulder.

TABLE 2

Structural characteristics of model Mn oxides, as identified by comparing the experimental results of Table 1 with the reference data indicated

Oxide	Structural characteristics	Reference data	
		XRD	IR
MnO	Manganosite: cubic system	JCPDS 7-0230	Vratny et al. [16]
Mn_3O_4	Hausmannite: tetragonal system	JCPDS 24-0734	Ishii et al. [17]
Mn_2O_3	α-Modification, Bixbyite-like: cubic system	JCPDS 31-0825	White and Keramidas [18]
MnO_2	β-Modification, pyrolusite-like: tetragonal system	JCPDS 24-0735	Potter and Rossman [19]

gives the structural characteristics for the model oxides, by comparing the experimental results (Table 1) with the reference XRD and IR data quoted.

Precursor compounds

The synthesized precursor compounds, **MnIII** and **MnVII** were subjected to IR and XRD examinations for verification. The results are shown in Figs. 1 and 2, respectively. A computer-oriented match with the JCPDS standard data attributes the XRD pattern of **MnIII** (Fig. 1(B)) to γ-Mn_2O_3 and/or Mn_3O_3 phases. The corresponding IR spectrum (Fig. 1(C)) displays weak absorptions at 1380 and 835 cm^{-1} due to NO_3^- contaminant (see Experimental, above), together with absorptions at 975, 623, 506, 418 and 352 cm^{-1}. The latter set of absorptions are well within the frequency range of Mn–O lattice vibrations [20]. A more detailed examination may disclose that they bear a great deal of similarity to the absorptions shown by the model Mn_3O_4 compound (Table 1). In the ν(OH) stretching region at >3200 cm^{-1} (not shown), a broad, weak absorption was observed at around 3412 cm^{-1}, due to associated hydroxyl groups. It relates to a very weak absorption at 1630 cm^{-1}, assignable to the δ(OH) vibration of water molecules [21]. No detectable absorptions were observed at >3500 cm^{-1}, thus excluding the presence of free hydroxide ions [21].

The results of the XRD and IR examinations of **MnVII** are shown in Fig. 2. Because no standard data have hitherto been reported by the JCPDS for NH_4MnO_4, the XRD pattern (Fig. 2(A)) was matched with standard patterns of the analogously structured $KMnO_4$ and NH_4ClO_4. The match results are given in Fig. 2(B). A few unmatched lines, two of them noted in Fig. 2(B), were found to coincide with characteristic lines of α-Mn_2O_3. Accordingly, one may envisage the occurrence of a limited redox reaction between MnO_4^- and Cl^- or NH_4^+. The corresponding IR spectrum (Fig. 2(C)) displays a strong absorption at 1390 cm^{-1} and a composite absorption of four ill-resolved maxima at 925, 910, 895 and 840 cm^{-1}. In the high-frequency region (not shown), a strong, broad absorption was observed centred around 3150 cm^{-1}. The latter absorption and that at 1390 cm^{-1} are assignable to the ν_3 and ν_4 modes of vibration of NH_4^+ ions [22], respectively. No NH_4^+ absorptions were observed in the range 1900–1700 cm^{-1}, thus indicating that it is freely rotating [23]. The absorptions at 925–840 cm^{-1} are almost identical to those observed by Baran and Aymonino [23] for the permanganate ion of NH_4MnO_4. The authors [23] assigned these absorptions to split ν_3 (925, 910 and 895 cm^{-1}) and ν_1 (840 cm^{-1}) modes of vibration of the permanganate ion. A similar set of absorptions is observed for the permanganate ions of $KMnO_4$, but at slightly different frequency values (namely, 924, 909, 900 and

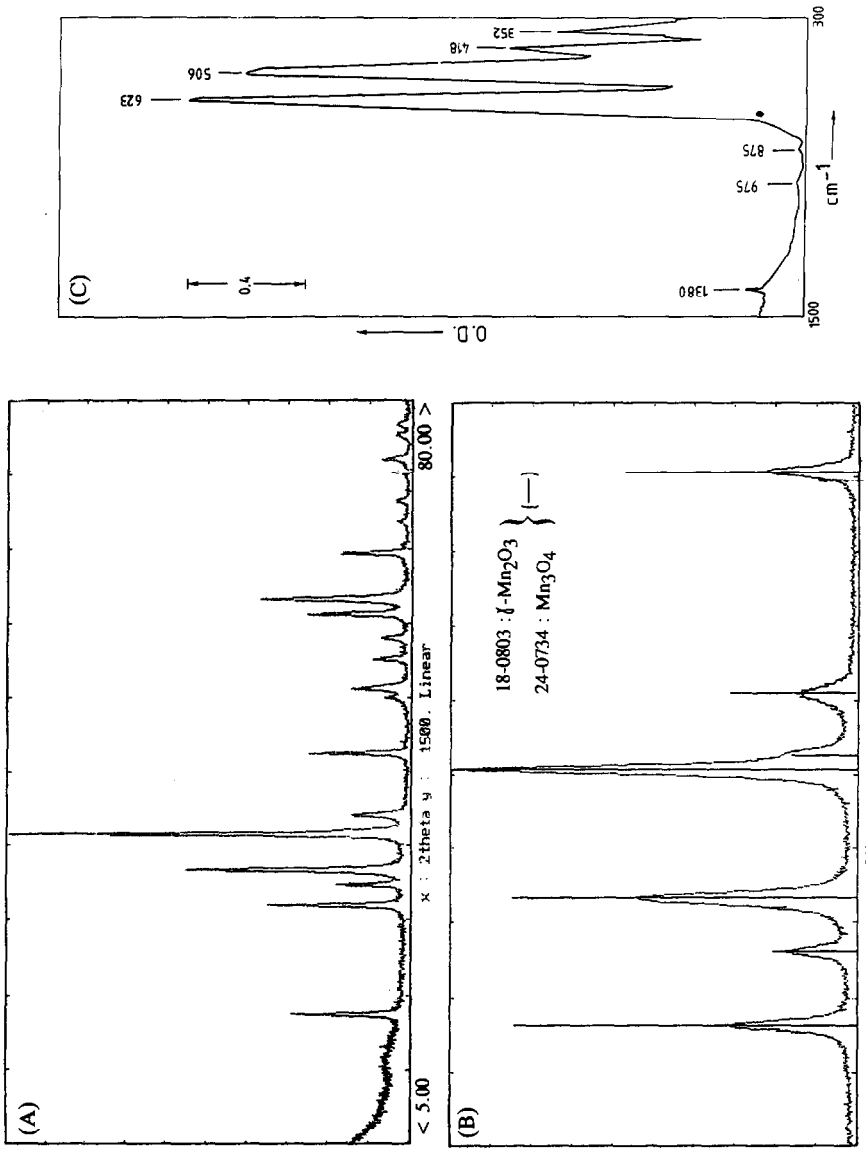

Fig. 1. XRD pattern (A) and IR spectrum (C) obtained for the precursor **MnIII**. The automatic match of the diffraction pattern is partly represented in (B).

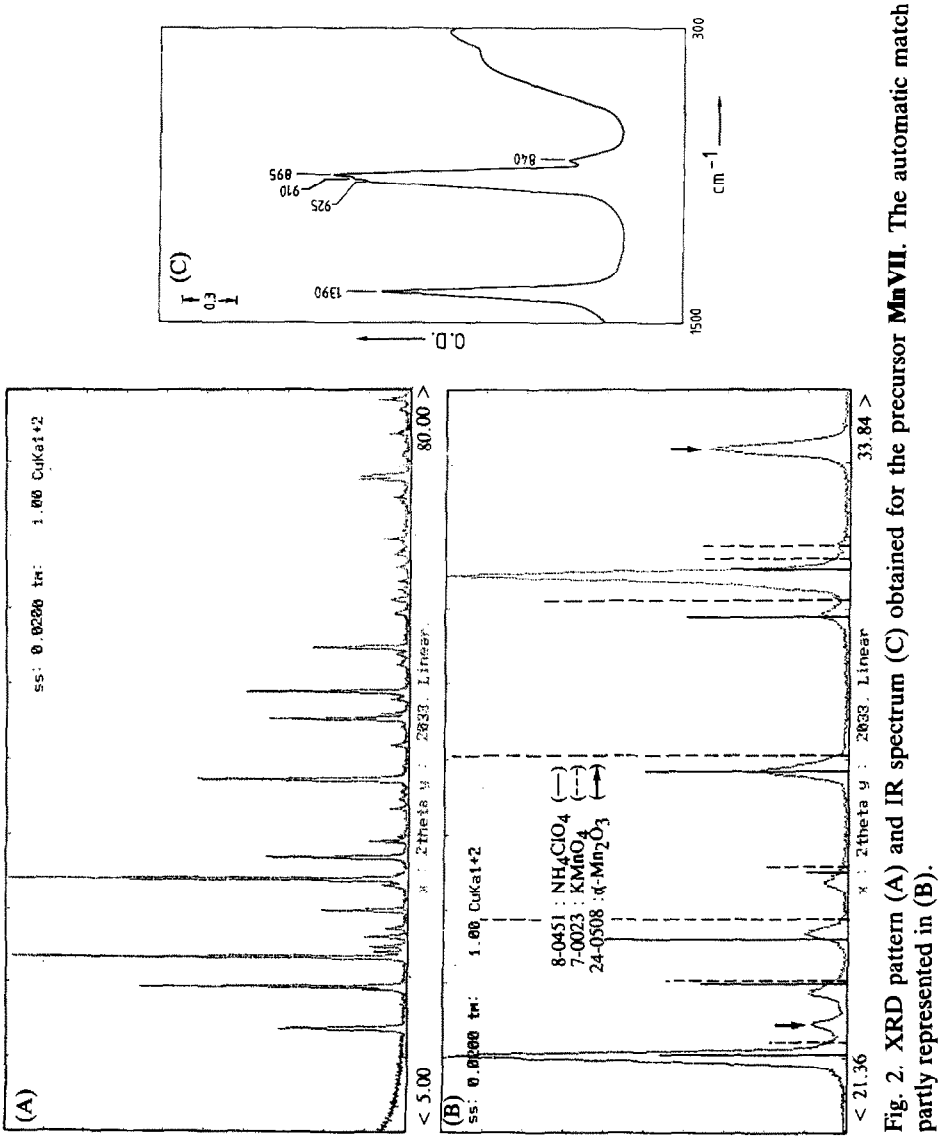

Fig. 2. XRD pattern (A) and IR spectrum (C) obtained for the precursor **MnVII**. The automatic match of the diffraction pattern is partly represented in (B).

840 cm^{-1}). These subtle, but significant, frequency differences have been ascribed [23] to the different symmetries of MnO_4^- in NH_4MnO_4 (T_d) and $KMnO_4$ (C_s).

Thermal analysis was performed on **MnII**, **MnIII** and **MnVII**, in air and N_2 atmospheres. Figure 3 shows the results obtained for the latter two precursors. The TG curve obtained for **MnII**, whether in air or N_2, monitored two weight-loss (WL) steps maximized at 180 and 250°C. The former step (90–210°C) caused 68% WL, and was shown by the DTA curve to involve three endothermic processes (at 110, 190 and 205°C). The latter WL step (at 480–570°C) was associated with 8.5% WL and a broad, but weak, endotherm centred around 550°C. Thus, the former step is composite in nature, whereas the latter is a simple step.

The TG results obtained for **MnIII** (Fig. 3) reveal that the decomposition occurs rapidly up to 160°C, and slows down markedly at higher temperatures. Correspondingly, the DTA curve (Fig. 3) displays a strong

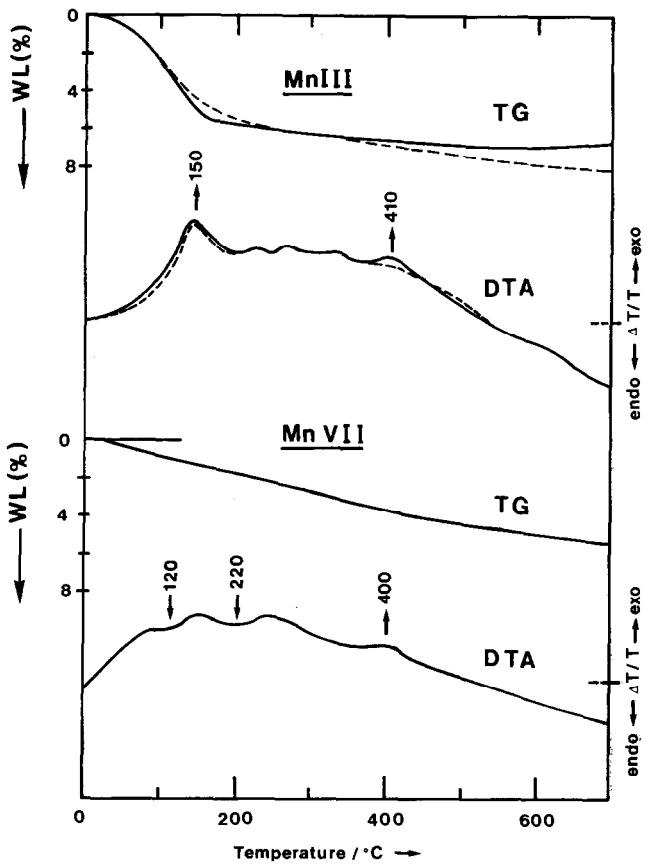

Fig. 3. TG and DTA curves obtained in air (——) and N_2 (– – –) atmospheres (20 ml min^{-1}) for untreated **MnIII** and the 120°C decomposition product of **MnVII**.

exotherm at 150°C, a moderate exotherm at 410°C, and a number of ill-defined weak exotherms at 200–350°C. The total WL (at 700°C) amounts to 7.2% in air, but to 8% in N_2. This inconsistency must be related to the minute weight gain observed in air above 600°C.

However, the TG curve obtained for **MnVII** (Fig. 3), or more precisely for its decomposition product at 120°C, is ill-defined throughout the temperature range examined, with a total WL of 5.8% at 700°C. The corresponding DTA curve (Fig. 3), however, indicates two very weak endotherms at 120 and 220°C, as well as a weak exotherm at 400°C. In contrast to the case with **MnIII**, these results were independent of the nature of the surrounding atmosphere (air or N_2).

Calcination products

The calcination products of the three precursors at 150, 300 and 600°C were subjected to XRD and IR examinations. The spectra obtained are exhibited in Figs. 4–7. The chemical and phase compositions derived therefrom are set out in Table 3.

The XRD diffractograms of **MnII(150)** and **MnII(300)** are largely similar (Fig. 4(A)), but distinctively different from that shown by **MnII(600)**. This does not seem to apply to the corresponding IR spectra (Fig. 5(A)): the spectra of the former two products are not so similar. The automatic match of the XRD patterns with the JCPDS standards is given in Figs. 4(B) and 4(C). For the **MnII** series, the bulk compositions revealed from the XRD and IR results are given in Table 3.

Figure 6(A) compares the XRD patterns of the calcination products of **MnIII**. It indicates that the pattern of **MnIII(300)** involves all of the lines shown in the pattern of **MnIII(150)**. However, there are also a few additional weak lines. However, **MnIII(600)** exhibits a considerably different pattern (Fig. 6(A)). It is worth noting that **MnIII(150)** has the same diffraction pattern as the precursor compound (Fig. 1(A)). This also applies to their IR spectra, except for a few minor differences. Therefore, Fig. 5(B) only shows the IR spectra of the 300°C and 600°C calcination products. The spectra accord with the XRD results, in exhibiting significantly different band structures for **MnIII(300)** and **MnIII(600)**. Conversely, however, the spectra of **MnIII(150)** and **MnIII(300)** are not as similar as the corresponding XRD patterns. The XRD match is given in Figs. 6(B) and 6(C). The bulk compositions deduced are given in Table 3.

The XRD diffractograms obtained for the calcination products of **MnVII** are compared in Fig. 7(A). It can be observed that each of the diffractograms involves two different, but inter-related patterns; one of them develops at the expense of the other with temperature increase. The automatic match (Figs. 7(B) and 7(C)) emphasizes this observation. The

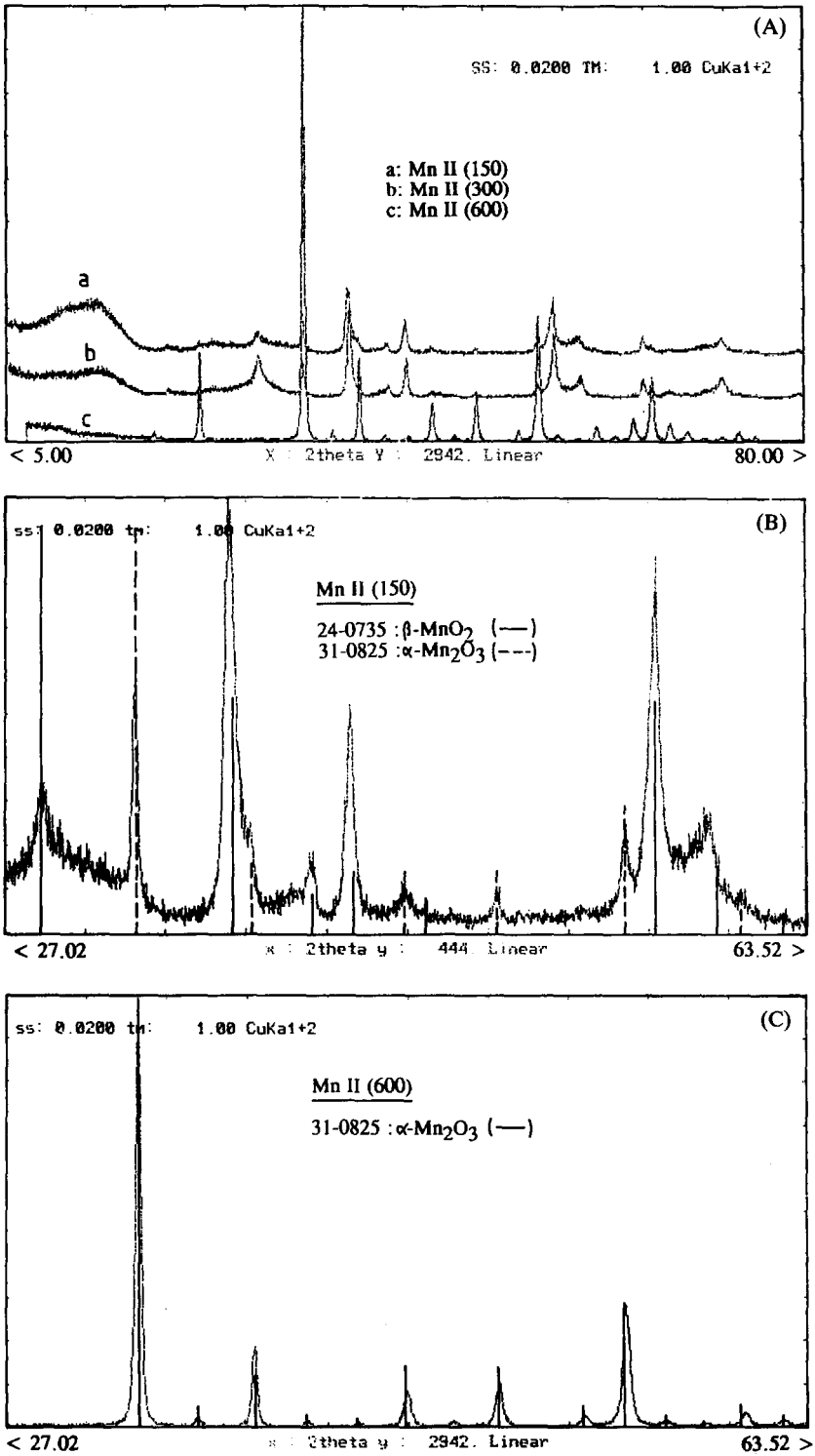

Fig. 4. XRD patterns exhibited by the calcination products of **MnII** (A). The automatic match of the patterns shown by the 150°C and 600°C products are respectively represented in (B) and (C).

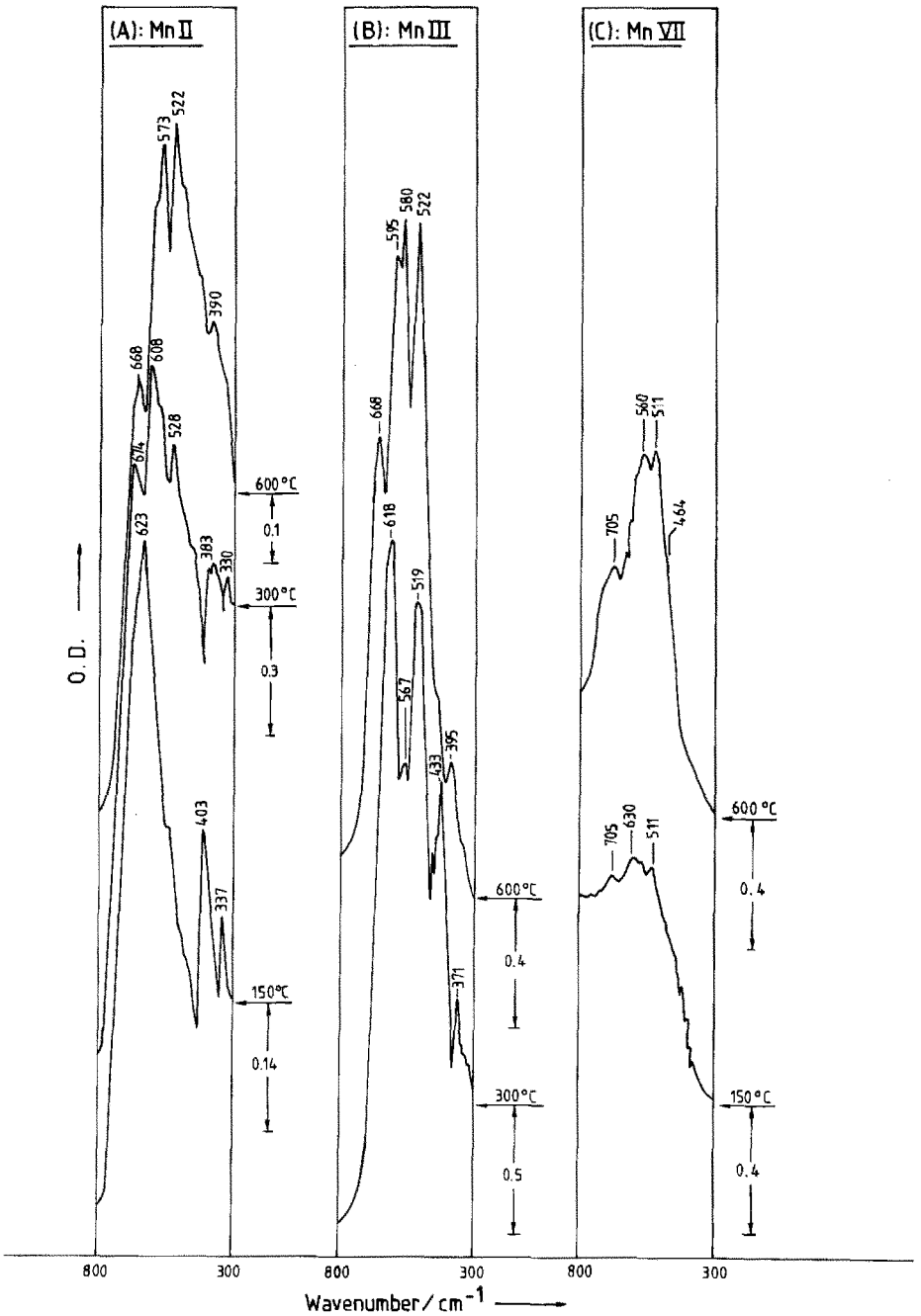

Fig. 5. IR spectra for the calcination products of **MnII** (A), **MnIII** (B) and **MnVII** (C) at the temperatures indicated.

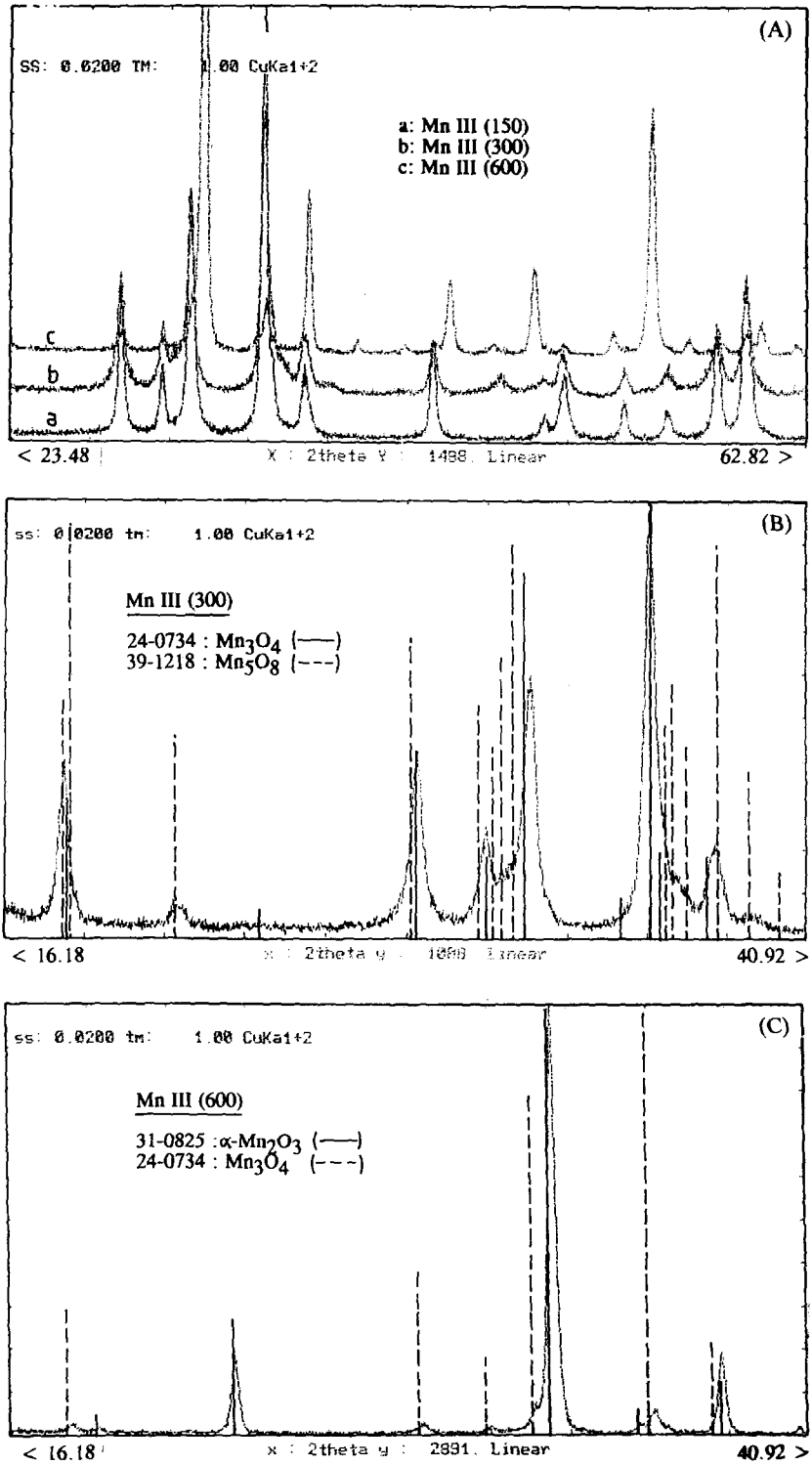

Fig. 6. XRD patterns exhibited by the calcination products of **MnIII** (A). The automatic match of the patterns shown by the 300°C and 600°C products are respectively represented in (B) and (C).

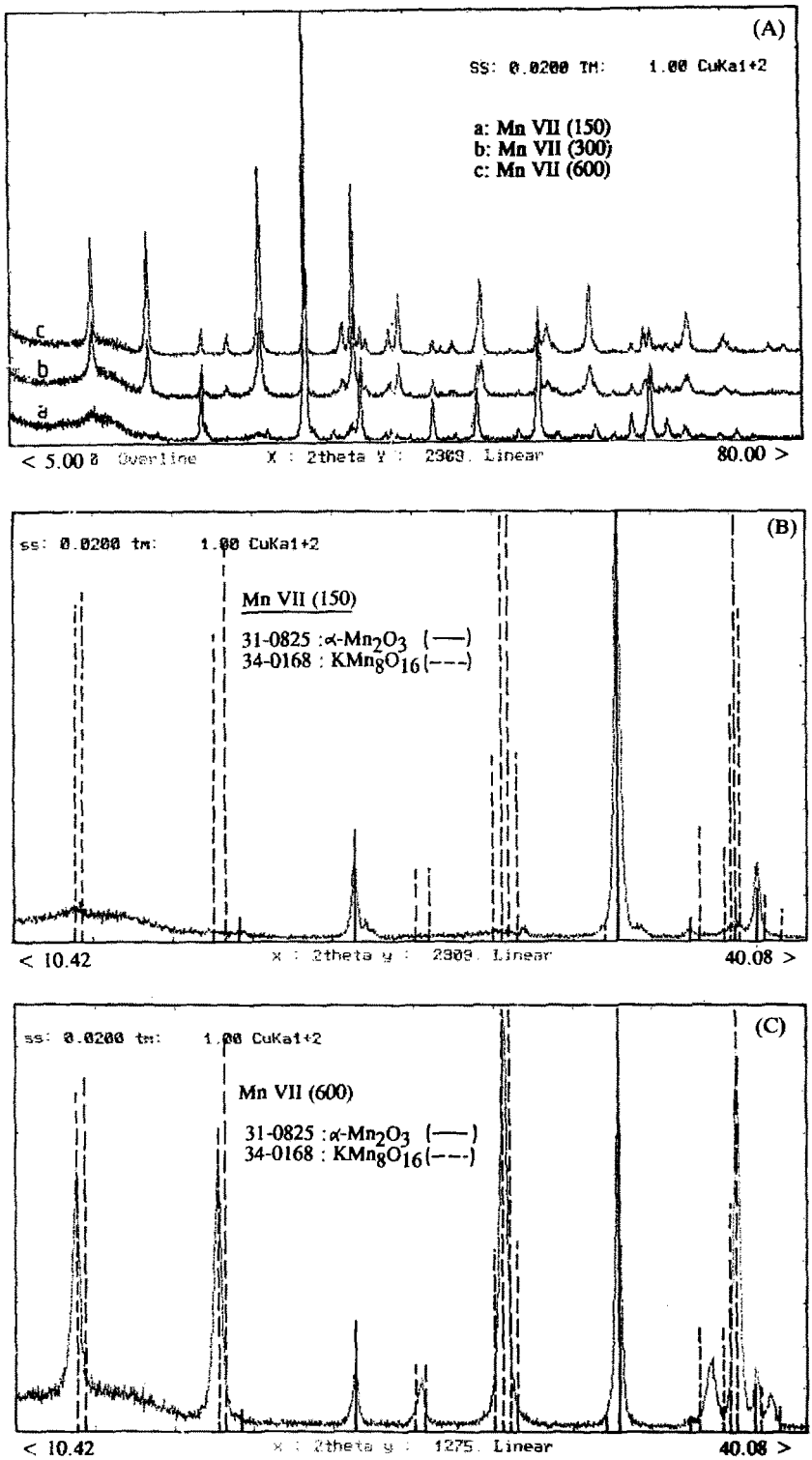

Fig. 7. XRD patterns exhibited by the calcination products of **MnVII** (A). The automatic match of the patterns shown by the 150°C and 600°C products are respectively represented in (B) and (C).

TABLE 3

Chemical and phase compositions of the crystalline bulk of the calcination products

Calcination product	Composition		
	Chemical	Phase [a]	Proportion
MnII(150)	MnO_2	β	Major
	Mn_2O_3	α	Minor
MnII(300)	MnO_2	β	Major
	Mn_2O_3	α	Minor
MnII(600)	Mn_2O_3	α	Sole
MnIII(150)	Mn_3O_4	Hausmannite	Sole
MnIII(300)	Mn_3O_4	Hausmannite	Major
	Mn_5O_8	Manganoxide (layer structure)	Minor
MnIII(600)	Mn_2O_3	α	Major
	Mn_3O_4	Hausmannite	Minor
MnVII(150)	Mn_2O_3	α	Dominant
MnVII(300)	Mn_2O_3	α	Major
	KMn_8O_{16}	Cryptomelane (Hollandite-group)	Minor
MnVII(600)	Mn_2O_3	α	Almost equal proportions
	KMn_8O_{16}	Cryptomelane	

[a] For α and β, see Table 2.

corresponding IR spectra are demonstrated in Fig. 5(C), and the bulk compositions are given in Table 3.

DISCUSSION

MnII → MnO_x

The thermal analysis (TG and DTA) indicated that on heating **MnII** ($Mn(NO_3)_2 \cdot 6H_2O$), the material melts near 90°C, but commences decomposition near 110°C. The decomposition process ceases near 210°C, at which temperature the TG curve determined a WL of 68%. The WL observed is slightly less than that expected (69.7%) from the $Mn(NO_3)_2 \cdot 6H_2O \rightarrow MnO_2$ transformation. Indeed, the XRD results (Fig. 4(B) and Table 3) confirm the formation of β-MnO_2 as a major phase in both **MnII(150)** and **MnII(300)**. In addition, α-Mn_2O_3 was detected, but as a minor phase. The characteristics of the structural modifications assumed by the two oxides are given in Table 2. Although the XRD patterns of both **MnII(150)** and **MnII(300)** are similar, the corresponding IR spectra (Fig. 5(A)) may reveal a slight enhancement of the characteristic absorptions of α-Mn_2O_3 with temperature increase. In terms of the

results available, it is hard to determine whether the β-MnO_2 and α-MnO_2 are produced simultaneously, or if the former is the precursor for the latter. It is certain, however, that no other MnO_x phases are detectable.

On further heating up to 700°C, the TG and DTA curves monitored an endothermic WL of 8.5%, maximized at 520–550°C. Correspondingly, the XRD (Fig. 4(C)) and IR (Fig. 5(A)) analyses of **MnII(600)** indicate complete decomposition of β-MnO_2 and the presence of α-Mn_2O_3 as the sole detectable phase. In fact, the $MnO_2 \rightarrow Mn_2O_3$ conversion is expected to result in a WL (9.2%) that is slightly higher than that determined by TG (8.5%).

The above results imply that $Mn(NO_3)_2 \cdot 6H_2O$ decomposes at 110–210°C to give predominantly β-MnO_2, thus encompassing an oxidation process. Increasing the temperature up to 600°C completely converts β-MnO_2 into α-Mn_2O_3, in a weight variant process maximized at 520–550°C. It is worth noting that the same thermal behaviour was observed irrespective of the nature of the heating atmosphere (air or N_2). This may suggest that the initial oxidation of Mn^{2+} is ascribed to the oxygen supplied by the decomposing NO_3^-, rather than to atmospheric oxygen. A corresponding exotherm may be hidden by the overlapping, strong endotherms associated with simultaneously occurring decomposition processes, e.g. the dehydration process).

MnIII → MnO_x

The preparation route for **MnIII** was originally chosen in the hopes of yielding an "Mn(III) oxyhydroxide". This was based on previous reports, e.g. ref. 8, which suggest that $Mn(OH)_2$, obtained via alkalization of aquated Mn^{2+} ions in ambient air atmosphere, is quantitatively oxidized to Mn^{3+} in the immediate vicinity of its formation. However, the present product exhibited an XRD pattern (Fig. 1(A)) that was fairly consistent with the standard patterns of γ-Mn_2O_3 and Mn_3O_4 (Fig. 1(B)). These results agree with the fact that γ-Mn_2O_3 and Mn_3O_4 exhibit almost identical XRD patterns [6]. In contrast, however, the IR spectrum of **MnIII** (Fig. 1(C)) displays absorptions assignable to Mn_3O_4 (see Table 1). According to Subba Rao et al. [24], the characteristic spectrum of γ-Mn_2O_3 is distinctively different: it displays absorptions at 673 (w, sp), 625 (sh), 608 (s, b), 500 (m, b), 385 (w, sp), 375 (w, sp) and 320 (s, b). Although both γ-Mn_2O_3 and Mn_3O_4 are similar in having spinel lattices [6], the co-existence of Mn^{2+} and Mn^{3+} ions in the lattice of the latter facilitates vibration coupling [17, 25]. Such a coupling has been found [17, 25] to be responsible for the distinctively strong, well-resolved absorptions of Mn_3O_4 at 700–500 cm^{-1} (Fig. 1(C) and Table 1).

The rapid decomposition step observed in the TG curve of **MnIII** at <200°C (Fig. 3) was accompanied by a WL (5.8%) that is much lower than would be expected (10.2%) for the elimination of one mole of water. This gives strong support to the XRD and IR results discussed above, in demonstrating that **MnIII** is not MnO(OH) ($2MnO(OH) = Mn_2O_3 \cdot H_2O$). The exothermic nature of the step (DTA, Fig. 3) may account for the involvement of some sort of oxidative WL processes. **MnIII** is highly contaminated with NO_3^-, the decomposition of which is usually oxidative [26]. The moderate exothermic process peaking at 410°C in air (Fig. 3), which marks the commencement of an obvious deviation between the weight losses determined in air and N_2, is largely retrogressed in the N_2 atmosphere. Thus, it most probably arises from an oxidation process involving atmospheric oxygen. As the temperature is increased in air, the slight WL detected in N_2 (1.8% at 350–700°C) is completely compensated for. This may occur via a weight-gain process, most probably due to oxygen uptake.

The XRD (Fig. 6) and IR (Fig. 5(B)) analyses results of **MnIII** calcination products indicate (Table 3) that Mn_3O_4 is still the sole detectable phase in **MnIII(150)**, but that it co-exists with minor Mn_5O_8 in **MnIII(300)**. A radical change is brought about by calcination at 600°C, where most of the product **(MnIII(600))** is shown to be composed of α-Mn_2O_3.

In view of the above results, it is obvious that the initial Mn^{2+} ions (coming from $Mn(NO_3)_2 \cdot 6H_2O$) were not quantitatively oxidized to the trivalent state. The product Mn_3O_4 includes Mn in both the divalent and trivalent states ($(Mn^{2+}(Mn^{3+})_2O_4$ [27]). Upon increasing the temperature up to 300°C, Mn_3O_4 is partially converted to Mn_5O_8 ($Mn_2^{2+}Mn_3^{4+}O_8$, manganoxide [28]). With further increase of temperature up to 600°C, Mn_5O_8 becomes undetectable, Mn_3O_4 becomes a minor component, and α-Mn_2O_3 emerges as the major phase (Table 3). These phase composition modifications may explain the exothermic weight gain monitored in the TG curve at 350–700°C (Fig. 3). The proposed oxygen uptake (see above) can contribute to the oxidation of Mn_3O_4 to Mn_5O_8, the latter probably being the intermediate to the formation of α-Mn_2O_3 at higher temperature.

MnVII → MnO_x

Analysis results for the precursor **MnVII** indicate (Fig. 2) that the material is predominantly NH_4MnO_4. However, the analysis of its calcination products (Table 3) reveals the existence of minor KMn_8O_{16} (cryptomelane), which develops progressively with temperature increase. A preliminary chemical analysis of **MnVII** yielded 3.6 wt.% K^+. The

inclusion of K^+ contaminant is inherent in the nature of the parent materials ($KMnO_4$ and NH_4Cl) employed in the preparation of **MnVII**.

The TG curve shown in Fig. 3 was not exhibited by **MnVII**, but by its decomposition product at 120°C (see Experimental). The ultimate WL determined at 700°C (5.4%) is much smaller than would be expected (42%) for the decomposition of untreated NH_4MnO_4. This indicates that the decomposition of the precursor is almost complete at 120°C, and the product (at 150°C) is shown (Table 3) to be mostly α-Mn_2O_3. A chemical analysis of a similar decomposition product [15] indicated the co-existence of very small amounts of MnO_2, NH_4NO_3, H_2O and molecularly adsorbed O_2. It must be the decomposition and elimination of these species that cause the extended, uneven WL monitored in the TG curve (Fig. 3). The corresponding DTA curve (Fig. 3) indicates that it is a composite process involving strongly overlapping endothermic (120 and 220°C) and exothermic (400°C) steps. The independence of the WL values on the nature of the surrounding atmosphere (air or N_2) is compatible with the low-temperature formation of α-Mn_2O_3 (at 120°C).

Upon increasing the calcination temperature up to 300°C, and further to 600°C, KMn_8O_{16} is formed and develops at the expense of α-Mn_2O_3 (See Fig. 7(B) and Table 3). For a hypothetical 4:1 mixture of Mn_2O_3 and KMn_8O_{16} (equal Mn proportions), the calculated K wt.% is 2.86% which is of the same order of magnitude as that found (3.6%). KMn_8O_{16} belongs to the Hollandite group [28], which includes channel-structured non-stoichiometric MnO_{2-x}. It has a defective structure $((V_{2-x}K_x^+)(Mn_{8-x}^{4+}Mn_x^{2+})O_{16}$, where V is a singly charged cationic vacancy [29]) stabilized by accommodating K^+ ions inside its large channels [29]. However, α-Mn_2O_3 is highly stoichiometric and thermally stable up to 1000°C [30]; it is normally non-oxidizable [31]. Therefore, it is tempting to suggest the formation of non-crystalline $KMnO_x$ species right from the beginning: it develops into the crystalline KMn_8O_{16} phase only at ≥300°C. This may explain the exotherm maximized at 400°C (DTA, Fig. 3). The fact that the XRD lines of α-Mn_2O_3 (Fig. 7(A)) weaken gradually as those of KMn_8O_{16} grow stronger may, however, suggest an alternative interpretation. The presence of K^+ ions may be seen to destabilize the structural integrity of α-Mn_2O_3, which is otherwise stable to calcination up to 1000°C. Hence, its consequent oxidation to KMn_8O_{16} at ≥300°C is made possible at the expense of a non-crystalline K-containing oxidant. Admittedly, however, the results here do not support any one of the two interpretations above the other.

CONCLUSIONS

The following conclusions can be drawn from the above presented and discussed results:

(1) The chemical and phase compositions of MnO_x are critically controlled by the nature of the precursor compound and the calcination temperature applied.

(2) $Mn(NO_3)_2 \cdot 6H_2O$ decomposes oxidatively at 110–210°C, leading to the formation of β-MnO_2 (pyrolusite) together with minor α-Mn_2O_3 (Bixbyite-like). The latter phase develops with temperature increase, and becomes the sole detectable phase at 600°C. The initial oxidation is most likely facilitated by decomposing NO_3^- ions.

(3) Hausmannite-like Mn_3O_4 can be obtained at room temperature by a slow addition of aqueous Mn^{2+} ions to 6 M ammonia solution. It is stable to heating up to 150°C. Thereafter, it is largely converted into α-Mn_2O_3 at 600°C, via the intermediate Mn_5O_8 ($Mn_2^{2+}Mn_3^{4+}O_8$, manganoxide). The oxidation process involved, maximized near 410°C, is evidently facilitated by atmospheric oxygen.

(4) NH_4MnO_4 is almost completely decomposed at a temperature as low as 120°C, to produce α-Mn_2O_3 as sole crystalline phase. The existence of K^+ ion contaminant facilitates the development of cryptomelane-like crystalline $KMnO_{16}$ phase at $\geq$300°C.

(5) IR can clearly distinguish between the similarly structured γ-Mn_2O_3 and Mn_3O_4; γ-Mn_2O_3 was not detected at all.

ACKNOWLEDGEMENTS

A.K.H.N. thanks the Egyptian government for a grant (Channel System No. 11/2/130). M.I.Z. thanks the C.N.R.S. of France for a research associateship that made possible such a fruitful cooperation between the universities of Poitiers and El-Minia.

REFERENCES

1 K. Katz, Adv. Catal., 5 (1953) 177.
2 S. Hasegawa, K. Yasuda, T. Mase and T. Kawaguchi, J. Catal., 48 (1977) 125.
3 R. Prasad, L.A. Kennedy and E. Ruckenstein, Catal. Rev. Sci. Eng., 26 (1984) 1.
4 J.C. Nardi, J. Electrochem. Soc., 132 (1985) 1787.
5 S. Bach, J.P. Pereira-Ramos, N. Baffier and R. Messina, Electrochim. Acta, 36 (1991) 1595.
6 O. Bricker, Am. Mineral., 50 (1965) 1296.
7 R.G. Burns and V.M. Burns, in B. Schumm, Jr., H.M. Joseph and A. Kozawa (Eds.), 2nd Manganese Dioxide Symp., I.C. MnO_2 Sample Off., Cleveland, OH, USA, 1981, p. 97.
8 T.E. Moore, M. Ellis and P.W. Selwood, J. Am. Chem. Soc., 72 (1950) 856.
9 A.F. Wells, Structural Inorganic Chemistry, 4th edn., Clarendon Press, Oxford, 1975, pp. 458–461.
10 M. LeBlanc and G. Wehner, Z. Phys. Chem., 168 (1934) 59.
11 J.S. Anderson, Annu. Rep. Chem. Soc. London, 43 (1946) 104.
12 H.R. Oswald, W. Feitknecht and M.J. Wampetich, Nature, 207 (1965) 72.
13 K.M. Parida, S.B. Kanungo and B.R. Sant, Electrochim. Acta, 26 (1981) 435.

14 L.L. Bircumshaw and T.M. Taylor, J. Chem. Soc., 3 (1950) 653.
15 F.M. Radwan, A.M. Abdel-Hameed, M.R. Mahmoud and R.B. Fahin, J. Therm. Anal., 32 (1987) 883.
16 F. Vratny, M. Dilling, F. Gugliotta and C.N.R. Rao, J. Sci. Ind. Res., Sect. B, 20 (1961) 590.
17 M. Ishii, M. Nakahira and T. Yamanako, Solid State Commun., 11 (1972) 209.
18 W.B. White and V.G. Keramidas, Spectrochim. Acta, Part A, 28 (1972) 501.
19 R.M. Potter and G.R. Rossman, Am. Mineral., 64 (1979) 1199.
20 N.T. McDevitt and W.L. Baun, Spectrochim. Acta, 20 (1964) 799.
21 J.A. Gadsden, Infrared Spectra of Minerals and Related Compounds, Butterworths, London, 1975, p. 16.
22 K. Nakamato, Infrared and Raman Spectra of Inorganic and Coordination Compounds, 3rd edn., Wiley, New York, 1978, pp. 132–139.
23 V.E.J. Baran and P.J. Aymonino, Z. Anorg. Allg. Chem., 354 (1967) 85.
24 G.V. Subba Rao, C.N.R. Rao and J. Ferraro, Appl. Spectrosc., 24 (1970) 436.
25 V.A.M. Barbers, Phys. Status Solidi, 33 (1969) 563.
26 D.N. Todor, Thermal Analysis of Minerals, Abacus Press, Kent, UK, 1976, pp. 112–125.
27 J.B. Dunitz and L.E. Orgel, J. Phys. Chem. Solids, 3 (1957) 20; 3 (1957) 318.
28 W. Feitknecht, Pure Appl. Chem., 9 (1964) 423.
29 C. Frondel, U.B. Marvin and J. Ito, Am. Mineral., 45 (1960) 871.
30 O. Glemser, G. Gattow and H. Meisiek, Z. Anorg. Allg. Chem., 309 (1961) 1.
31 J. Lima-de Faria and A. Lopes-Vieira, Mineral. Mag., 33 (1964) 1024.